

2-2010

Phase stability and transformations in NiTi from density functional theory calculations

Karthik Guda Vishnu

Purdue University - Main Campus, karthikguda@purdue.edu

Alejandro Strachan

Purdue University - Main Campus, strachan@purdue.edu

Follow this and additional works at: <http://docs.lib.purdue.edu/nanopub>



Part of the [Nanoscience and Nanotechnology Commons](#)

Vishnu, Karthik Guda and Strachan, Alejandro, "Phase stability and transformations in NiTi from density functional theory calculations" (2010). *Birck and NCN Publications*. Paper 592.

<http://docs.lib.purdue.edu/nanopub/592>

This document has been made available through Purdue e-Pubs, a service of the Purdue University Libraries. Please contact epubs@purdue.edu for additional information.

Phase stability and transformations in NiTi from density functional theory calculations

Karthik Guda Vishnu^a, Alejandro Strachan^{a,b,*}

^a School of Materials Engineering, Purdue University, West Lafayette, IN 47907, USA

^b Birck Nanotechnology Center, Purdue University, West Lafayette, IN 47907, USA

Received 9 May 2009; received in revised form 1 September 2009; accepted 6 September 2009

Available online 10 November 2009

Abstract

We used density functional theory to characterize various crystalline phases of NiTi alloys: (i) high-temperature austenite phase B2; (ii) orthorhombic B19; (iii) the monoclinic martensite phase B19'; and (iv) a body-centered orthorhombic phase (BCO), theoretically predicted to be the ground state. We also investigated possible transition pathways between the various phases and the energetics involved. We found B19 to be metastable with a 1 meV energy barrier separating it from B19'. Interestingly, we predicted a new phase of NiTi, denoted B19'', that is involved in the transition between B19' and BCO. B19'' is monoclinic and can exhibit shape memory; furthermore, its presence reduces the internal stress required to stabilize the experimentally observed B19' structure, and it consequently plays a key role in NiTi's properties.

© 2009 Acta Materialia Inc. Published by Elsevier Ltd. All rights reserved.

Keywords: NiTi; Martensitic phase transformation; Density functional theory (DFT); Shape memory alloys (SMA)

1. Introduction

Shape memory alloys are an important class of active materials with applications ranging from medicine to aerospace due to two unique properties: (i) the ability to recover their original shape after large deformations; and (ii) superelasticity, or the ability to recover very high amounts of strain upon unloading. Both these properties stem from a solid-to-solid martensitic (diffusionless) phase transformation from a high-temperature austenite phase to a martensitic phase of lower symmetry. A number of materials are known to exhibit shape memory, including NiTi, AuCu and MnCu [1], with NiTi, commercially known as Nitinol, being the most widely used today. Such choice is due to several desirable properties, like high damping capacity, resistance to corrosion and abrasion, high tensile strength

and excellent biocompatibility [1–4]. Despite the technological importance of shape memory materials and recent advances, the fundamental mechanisms that govern their unique behavior are not fully known. While the martensitic transformation governing the thermo-mechanical response of these materials at the macroscale is well characterized [5] and the theoretical framework to understand shape memory and the atomic-scale reversibility of phase transformations in terms of the symmetry of the phases involved is in place [6], the complex phenomena that emerge from many-body atomic processes are not fully understood for real materials. For example, the role of microstructure and internal stresses in the stabilization of the martensite phase in NiTi remains unknown.

Density functional theory calculations provide valuable information to fill this gap in knowledge [7–11], but additional work is still needed to obtain a full picture of the atomic structure and microstructure of these materials. Using density functional theory (DFT), Huang et al. [8] predicted the zero temperature ground state of NiTi to be a body-centered orthorhombic (BCO) structure belonging

* Corresponding author. Address: School of Materials Engineering, Purdue University, West Lafayette, IN 47907, USA. Tel./fax: +1 765 496 3551.

E-mail address: strachan@purdue.edu (A. Strachan).

to space group 63 (B33). This finding is particularly important since the BCO structure cannot store shape memory due to its symmetry. In other words, the $B2 \rightarrow BCO \rightarrow B2$ transformation is not reversible at the atomic level. Huang et al. proposed that the observed monoclinic phase (B19') is stabilized by the internal stresses associated with the complex martensitic microstructure. More recently, Wang [9] predicted B19' to be metastable and separated from BCO by an energy barrier of 0.02 eV per formula unit using nudged elastic band with DFT [12,13] calculations. Kibey et al. [10] predicted an energy barrier of 13 meV per formula unit for the homogeneous transformation from B2 to B19.

We envision that large-scale molecular dynamics (MD) simulations with accurate interatomic potentials will play an important role in revealing the interplay between the microstructure that develops during the martensitic transformation, the associated internal stresses and the properties of the alloy. Despite being ideally suited for such tasks and the technological importance of NiTi alloys, very few studies have been conducted so far [14–17]; this is possibly due to the lack of accurate interatomic potentials that can capture the various phases of NiTi.

In this paper we use DFT with the generalized gradient approximation (GGA) to:

- (i) Characterize the atomic structure, relative stability of the various crystal structures believed to govern the behavior of NiTi alloys.
- (ii) Characterize plausible pathways for homogeneous transitions between the various phases and energetics involved.

The remainder of the paper is organized as follows: Section 2 discusses the Computational methodology used. We present our results together with a discussion of their meaning in Sections 3, 4 and 5; finally, conclusions are drawn in Section 6.

2. Simulation details

We used SeqQuest [18–20], a density functional theory [21] code developed at Sandia National Laboratories with the generalized gradient approximation of Perdew, Burke and Ernzerhof (PBE) [22]. SeqQuest uses contracted Gaussian functions as a basis set and our calculations are performed with Double Zeta plus polarization basis sets. We used norm-conserving pseudo potentials of the Hamann type [23] to replace core electrons parameterized for the PBE functional. We used two pseudopotentials for titanium: a more accurate one that considers 3*p* electrons as part of the valence (denoted 3*p*6) and one where 3*p* states are considered part of the core (denoted 3*p*0). All the results in this paper correspond to calculations using the more accurate 3*p*6 Ti pseudopotential unless mentioned otherwise. We used a $14 \times 10 \times 10$ *k*-mesh for the B2 phase set in a tetragonal unit cell (four atoms), as shown in Fig. 1a, with cell vectors: $a = x[1\ 0\ 0]$, $b =$

$y[0\ 1\ 1]$, $c = z[0\ -1\ 1]$. We used the same *k*-mesh for all the other phases, as shown in Fig. 1(b–e). We performed all our calculations at 0.003 Ry (0.04 eV) electronic temperatures. All our calculations were spin independent. SeqQuest uses the maximum change in any Hamiltonian matrix element as its convergence criterion [18]. This was set to be 2.72×10^{-4} eV for all calculations. The initial SCF blend factor was set at 0.3.

All atomic configurations were fully relaxed by minimizing the energy using the Broyden method [24]. Convergence was assumed when the absolute value of the atomic force on every atom was less than or equal to 5×10^{-3} eV Å⁻¹. To relax the cell parameters we performed an optimization where the energy was minimized with respect to each degree of freedom in a sequential manner. Each cycle involved minimizing the energy with respect to: (i) volume, where all lattice parameters were changed with the same multiplicative factor; (ii) *b/c* at constant volume; (iii) *c/a* at constant volume; and (iv) monoclinic angle (γ) (for BCO phases described below). We performed these sequential optimization steps cyclically until the energy change was less than 0.2 meV per formula unit in one complete cycle.

3. Crystal structures and energetics

Depending on the thermo-mechanical treatments and the composition [5], the different phases that are relevant for NiTi (equiatomic) are as follows: (i) B2 (CsCl) is the austenite phase; (ii) B19 is an intermediate phase with an orthorhombic structure; and (iii) B19' is the martensite structure and has a monoclinic structure. However, Huang et al. [8] using DFT predicted a new body orthorhombic structure (BCO) to be the lowest energy (ground state) structure; BCO differs from B19' in the monoclinic angle as well as the internal atomic coordinates, and, due to its symmetry, it cannot exhibit shape memory. We also report a new phase with a monoclinic angle intermediate between B19' and BCO; this new phase, which will be denoted B19'' (and is described in Sections 4.3 and 5), has the same symmetry of B19' and, consequently, can exhibit shape memory behavior.

We obtained equilibrium structures for all phases by minimizing energy with respect to both atomic positions and cell parameters, as described in Section 2. These structures thus correspond to zero pressure and zero temperature (with the exception that zero point energy is not taken into account). Tables 1 and 2 summarize the structural properties of the various phases; they show the lattice parameters, relative energies and the internal atomic coordinates of the B2, B19, B19', B19'' and BCO phases. Our results compare well with previous experimental [25,26] as well as theoretical results [8,10]. X_{Ni} , Y_{Ni} , X_{Ti} and Y_{Ti} refer to fractional atomic displacements in the $x[1\ 0\ 0]$ and $y[0\ 1\ 0]$ directions with respect to B2 structure for nickel and titanium, respectively (refer to Fig. 1).

In agreement with prior ab initio simulations, we find B19' to be unstable with respect variations of its monoclinic

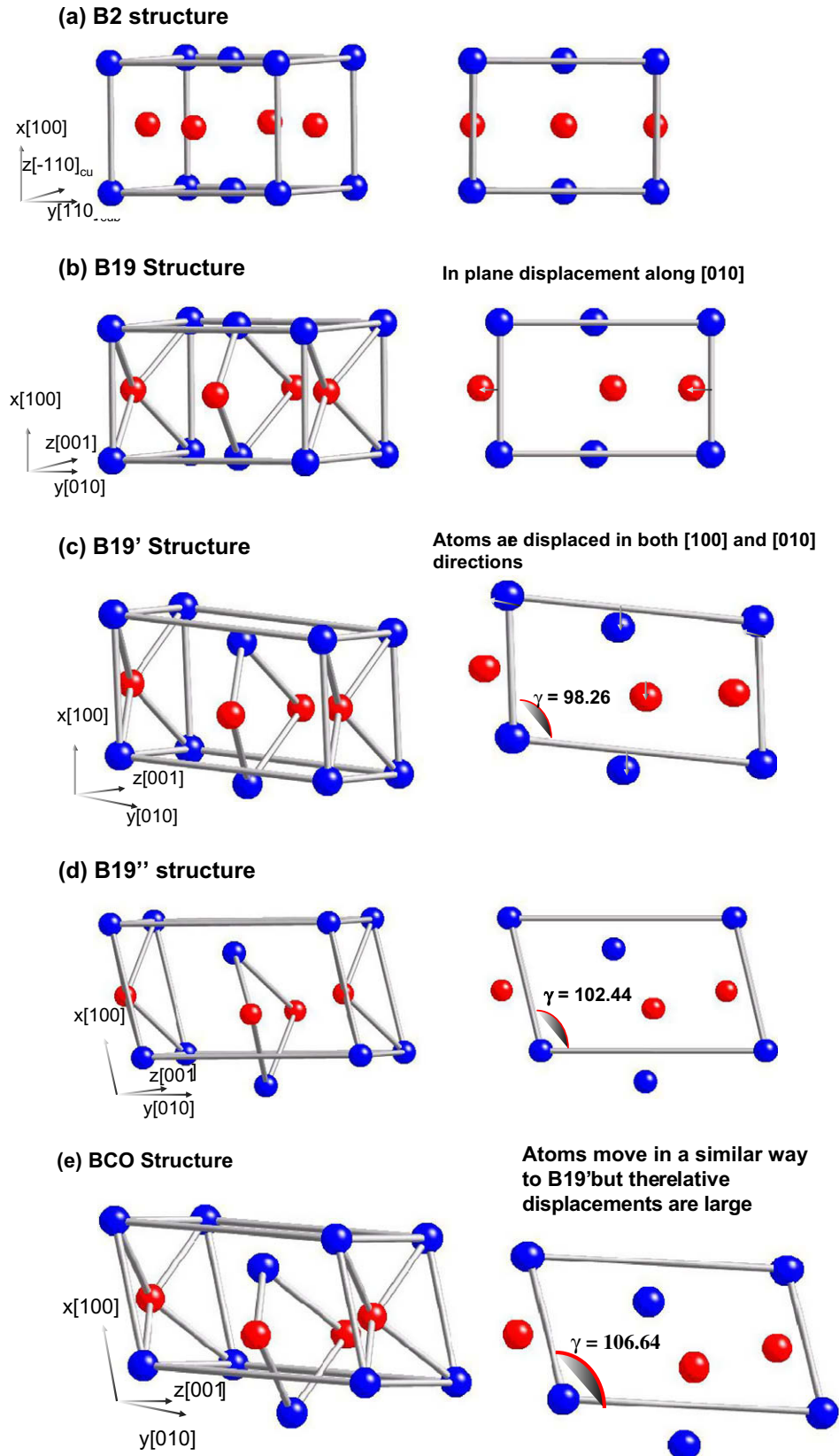


Fig. 1. Snapshots of the various crystal structures of NiTi. (a) B2 (austenite) four-atom unit cell, (b) B19, (c) B19' (martensite), (d) B19'' (new phase) and (e) BCO. Ti and Ni atoms are indicated by blue and red spheres, respectively.

angle when using the $3p6$ pseudopotential; interestingly, the $3p0$ calculations predict B19' to be metastable with an

equilibrium monoclinic angle of 98.26° . This angle is similar to the experimental one corresponding to the

Table 1

Lattice parameters and relative energy of B2, B19, B19', B19'' and BCO from our calculations (DFT–GGA) as well as previous experimental and theoretical work.

Phase	Method	a (Å)	b (Å)	c (Å)	γ (°)	$E - E_{B2}$ (eV)
B2	DFT–GGA–3p6	3.014	4.262	4.262	90.0	0.000
	DFT–GGA–3p0	3.009	4.255	4.255	90.0	0.000
	Exp. [24]	3.014	4.262	4.262	90.0	0.000
B2'	DFT–GGA–3p6	3.014	4.262	4.262	90.0	–0.008
	DFT–GGA–3p0	3.009	4.255	4.255	90.0	–0.009
B19	DFT–GGA–3p6	2.840	4.602	4.120	90.0	–0.053
	DFT–GGA–3p0	2.850	4.597	4.167	90.0	–0.051
B19'	DFT–GGA–3p6	2.933	4.678	4.067	98.26*	–0.081
	Exp. [25]	2.898	4.646	4.108	97.8°	–
	DFT–GGA–3p0	2.933	4.678	4.108	98.26°	–0.081
B19''	DFT–GGA–3p6	2.923	4.801	4.042	102.44°	–0.087
	DFT–GGA–3p0	2.926	4.819	4.034	103.20°	–0.093
BCO	DFT–GGA–3p6	2.928	4.923	4.017	106.64°	–0.092
	DFT–GGA–3p0	2.926	4.925	4.012	106.50°	–0.097
	DFT–GGA [8]	2.940	4.936	3.997	107.0°	–0.01

Energy is given per formula unit (NiTi).

* γ is constrained to 98.26°, which is the equilibrium angle of metastable B19' as predicted by the 3p0 pseudopotential.

Table 2

Fractional atomic coordinates for the various equilibration phases from our calculations (DFT–GGA) and previous theoretical calculations.

Phase	Method	X_{Ni}	Y_{Ni}	X_{Ti}	Y_{Ti}
B2	DFT–GGA–3p6	0.000	0.000	0.000	0.00
	DFT–GGA–3p0	0.000	0.000	0.000	0.000
	Exp. [24]	0.000	0.000	0.000	0.00
B2'	DFT–GGA–3p6	0.000	0.032	0.000	0.016
	DFT–GGA–3p0	0.000	0.034	0.000	0.013
B19	DFT–GGA–3p6	0.000	0.064	0.000	0.026
	DFT–GGA–3p0	0.000	0.067	0.000	0.033
B19'	DFT–GGA–3p6	0.045	0.076	0.089	0.033
	DFT–GGA–3p0	0.042	0.071	0.073	0.027
	Exp. [25]	0.037	0.074	0.082	0.034
B19''	DFT–GGA–3p6	0.064	0.079	0.115	0.037
	DFT–GGA–3p0	0.068	0.078	0.116	0.033
BCO	DFT–GGA–3p6	0.082	0.079	0.140	0.036
	DFT–GGA–3p0	0.084	0.079	0.140	0.036
	DFT–GGA [8]	0.086	0.077	0.142	0.036

X_{Ni} , Y_{Ni} , X_{Ti} and Y_{Ti} indicate the displacements of nickel and titanium atoms in the a and b directions, respectively, relative to B2.

martensitic phase; thus, we fixed the monoclinic angle to this value and fully relaxed all the other structural and atomic coordinates to define B19' for the 3p6 pseudopotential.

4. Phase transformations

4.1. B2 to B19 phase transformation

We characterized the B2 to B19 transformation in two steps: (i) as reported earlier [7], the B2 phase is unstable with respect to atomic displacements along $[1\ 1\ 0]_{cubic}$ and the first step involves relaxing the structure with respect to atomic positions keeping the cell parameters at B2

values; (ii) lattice parameter deformation from a cubic system to an orthorhombic cell that involve stretching of $[1\ 1\ 0]_{cubic}$ and compression of other two lattice parameters. The first step can be characterized as purely displacive transformation and the second step involves both atomic movement and a change in lattice parameter.

As in Ref. [7], our calculations showed that the austenite phase (B2) is unstable with respect to atomic displacement along the $[1\ 1\ 0]_{cubic}$ direction. We found relaxed atomic coordinates for B2 lattice parameters performing an ionic relaxation starting with B19 fractional atomic coordinates. The resulting structure, denoted B2', had the symmetry of B19. As the first (purely displacive) step in the B2 – B19 transformation, we linearly interpolated the internal

atomic coordinates of nickel and titanium atoms between B2 ($\delta_{B2}^{Ni}, \delta_{B2}^{Ti}$) values and B2' ($\delta_{B2'}^{Ni}, \delta_{B2'}^{Ti}$) structures. This can be shown in the equation below:

$$\begin{aligned}\delta_{\lambda_1}^{Ni} &= \lambda_1 * \delta_{B2'}^{Ni} \\ \delta_{\lambda_1}^{Ti} &= \lambda_1 * \delta_{B2'}^{Ti}\end{aligned}\quad (1)$$

where λ_1 is a continuous reaction coordinate variable; $\lambda_1 = 0$ leads to the B2 structure and $\lambda_1 = 1$ gives the B2' structure. Fig. 2 shows total energy as a function of λ_1 between B2 and B2'; each point on this curve corresponds to a single point calculation showing the direct correlation between energy and atomic displacements. As pointed out previously in Ref. [7], such an energy landscape indicates that large atomic fluctuations around average equilibrium positions are to be expected in the B2 phase.

In order to study the transformation between B2' and B19, we linearly interpolated the lattice parameters of the two phases. The degree of transformation was then described by the reaction coordinate λ_2 , which determined the lattice parameters in the following way:

$$\begin{aligned}a(\lambda_2) &= a_{B19}\lambda_2 + a_{B2}(1 - \lambda_2) \\ b(\lambda_2) &= b_{B19}\lambda_2 + b_{B2}(1 - \lambda_2) \\ c(\lambda_2) &= c_{B19}\lambda_2 + c_{B2}(1 - \lambda_2)\end{aligned}\quad (2)$$

$\lambda_2 = 0$ gave the B2 structure and $\lambda_2 = 1$ gave the B19 structure. We performed a number of calculations varying λ_2 from -0.2 to 1.2 ; for each λ_2 we fully relaxed the structure with respect to electronic and ionic degrees of freedom, starting from B2' and B19 atomic coordinates. The resulting energetics as a function of λ_2 are shown in Fig. 2. We did not find a barrier between B2 and B19, which is in disagreement with Kibey et al. [10], who reported a barrier of 13 meV/NiTi between B2 and B19.

4.2. B19 to B19' phase transformation

We performed a similar analysis to characterize the homogeneous transformation between B19 and B19' (martensite) phases. We linearly interpolated between the lattice parameters of the B19 and B19' ground state struc-

tures and used the monoclinic angle (γ) as our reaction coordinate (λ_3). The angle varied from 90° for B19 to 98.26° for B19', and the cell vectors were given as a function of the reaction coordinate by:

$$\begin{aligned}a(\lambda_3) &= a_{B19'} \frac{\lambda_3 - \gamma_{B19}}{\gamma_{B19'} - \gamma_{B19}} + a_{B19} \frac{\gamma_{B19'} - \lambda_3}{\gamma_{B19'} - \gamma_{B19}} \\ b(\lambda_3) &= b_{B19'} \frac{\lambda_3 - \gamma_{B19}}{\gamma_{B19'} - \gamma_{B19}} + b_{B19} \frac{\gamma_{B19'} - \lambda_3}{\gamma_{B19'} - \gamma_{B19}} \\ c(\lambda_3) &= c_{B19'} \frac{\lambda_3 - \gamma_{B19}}{\gamma_{B19'} - \gamma_{B19}} + c_{B19} \frac{\gamma_{B19'} - \lambda_3}{\gamma_{B19'} - \gamma_{B19}}\end{aligned}\quad (3)$$

where γ_x is the equilibrium monoclinic angle of phase B19' as predicted by our calculations with the $3p0$ pseudopotential. The energetics involved in the B19 \rightarrow B19' transformation are also shown in Fig. 2 as a function of the reaction coordinate; for each value of λ_3 we plotted the energy after relaxation with respect to electronic and ionic degrees of freedom. Our calculated energy landscape indicates the presence of a small barrier (1 meV) between the two phases. Huang et al. [8] also studied the transition between B19 and B19' and reported no barrier; however, this transition was not the main focus of their work and no data points were shown in the $90^\circ < \gamma < 94^\circ$ range. We predicted the maximum to correspond to $\gamma = 90.8^\circ$. This is a significant result as it shows that the orthorhombic B19 structure is metastable in the equiatomic alloy of NiTi without the presence of impurities.

4.3. B19' to BCO phase transformation

To characterize the transformation between the martensite phase (B19') and BCO we used a linear interpolation in lattice parameters similar to our approach for the transformations discussed above. As in the B19 \rightarrow B19' case, the angle γ was used as the reaction coordinate. For each angle we minimized the structures with respect to electronic and ionic degrees of freedom starting from both the B19' and BCO fraction atomic positions. The energetics involved in this transformation are shown in Fig. 3a. B19' is unstable with respect to the monoclinic angle (γ) and the transformation from B19' to BCO does not involve any barrier. This is in agreement with Huang et al. [8], who predicted a similar behavior using a number of variations of DFT. Fig. 3b shows the equilibrium fractional atomic coordinates of the lowest energy configuration as a function of monoclinic angle (γ); it is clear that our DFT-GGA calculations find an intermediate phase between B19' and BCO, predicted to be stable for angles between 100° and $\sim 104^\circ$. As will be described below, the intermediate phase is also monoclinic and belongs to the same space group as B19', so we will refer to it as B19''. To characterize the properties of these three phases, we fitted the observed internal coordinates as a function of monoclinic angle using linear functions and extrapolated these functions to obtain information for each phase for a wider range of monoclinic angle. Fig. 3c and d shows, respectively, the energy and shear stress in the plane of monoclinic angle

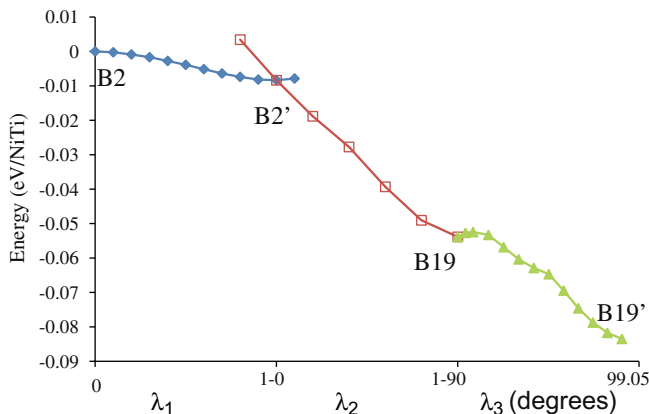


Fig. 2. Energy per formula as a function of reaction coordinate for the B2 \rightarrow B19 and B19 \rightarrow B19' transformation.

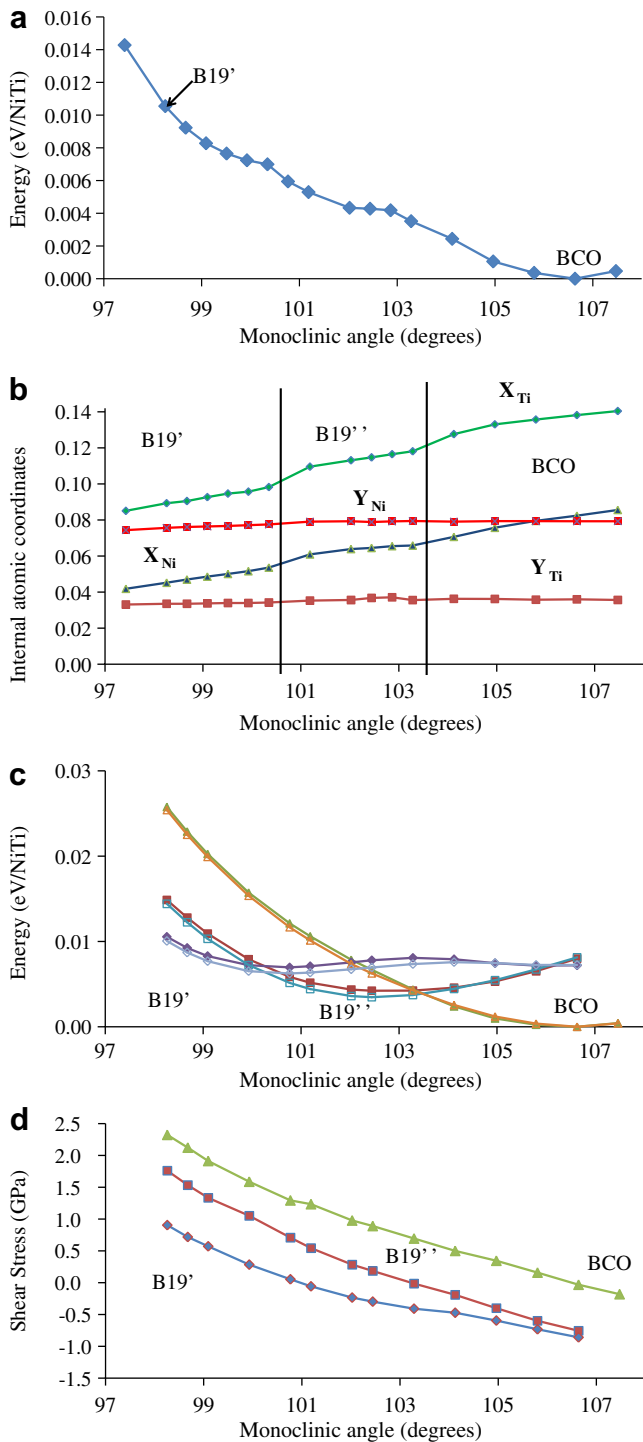


Fig. 3. (a) Variation of energy per NiTi with monoclinic angle (γ). (b) Variation of fraction coordinates for Ni and Ti atoms with monoclinic angle (γ). The three branches demarcated by vertical lines belong to the three different low-energy phases. (c) Energy (eV/NiTi) as a function of monoclinic angle for B19', B19'' and BCO with monoclinic angle (γ). Full symbols indicate that the calculations are done with a $14 \times 14 \times 14$ k -mesh and empty symbols indicate that they are done with a $22 \times 22 \times 22$ k -mesh with respect to cubic unit cell. (d) Variation of shear stress (GPa) with monoclinic angle (γ). B19'' phase reduces the stress required to stabilize the B19' phase.

(γ) as a function of angle for each phase. In order to verify the existence of B19'', we repeated the above calculations with a

denser k -grid of $22 \times 16 \times 16$. The open symbols in Fig. 3c refer to these calculations. As can be seen from Fig. 3c, the existence of B19'' does not depend on k -sampling. The new B19'' phase has an equilibrium monoclinic angle of 102.4° . The lattice parameters in this calculation were obtained from the linear interpolation between B19' and BCO phases; the results reported Tables 1 and 2 correspond to this relaxed structure. Note that the values reported in Tables 1 and 2 for B19' do not correspond to the minimum of the B19' branch of Fig. 3c, but we fixed the angle to that predicted for B19' by the $3p0$ pseudopotential calculations.

B19'' plays a key role in the transition from B19' to BCO as it is the lowest energy structure for angles between 100° and $\sim 104^\circ$. Fig. 3d shows that B19'' plays a key role in B19' being the observed phase and shape memory in NiTi since it leads to a significant decrease in the internal stresses required to stabilize B19'.

Our $3p0$ calculations using SeqQuest were very similar to those described above; those calculations, shown in detail in the supplementary material, predicted the B19'' phase to be stable over a range of monoclinic angles between B19' and BCO. We also performed calculations with abinit [27,28] – a DFT code that uses a plane wave basis set. These results, also described in the supplementary material, show only one monoclinic phase together with BCO; the predicted monoclinic phase has electronic properties and structural properties similar to the B19'' phase predicted by SeqQuest.

5. Properties of the low-energy phases of NiTi and shape memory

5.1. Atomic structure and symmetry of the low-energy phases

We now focus on the characterization of the structure and properties of the new structure, B19''. As the monoclinic angle (γ) is increased a point is reached when the structure becomes orthorhombic; this occurs when the parameter Δ in following equation goes to zero.

$$\Delta = a(\sin^2(180^\circ - \gamma) + \cos \gamma) + 2b \cos \gamma \quad (4)$$

Table 3 shows the Δ values for B19', B19'' and BCO. The results from our calculations are compared to those in Ref. [8] for B19' and BCO, and show that the new B19'' phase is monoclinic; our results also confirm the fact that the ground state structure of NiTi is orthorhombic. Like the B19' structure, B19'' exhibits a mirror plane and a screw axis normal to it, as well as an inversion center,

Table 3
Values of Δ for B19', intermediate and BCO.

Phase	Method	Δ (Å)
B19'	DFT-GGA-3p6	169×10^{-3}
	DFT-GGA [8]	176×10^{-3}
Intermediate	DFT-GGA-3p6	89×10^{-3}
	DFT-GGA [8]	11×10^{-3}
BCO	DFT-GGA-3p6	11×10^{-3}
	DFT-GGA [8]	6×10^{-3}

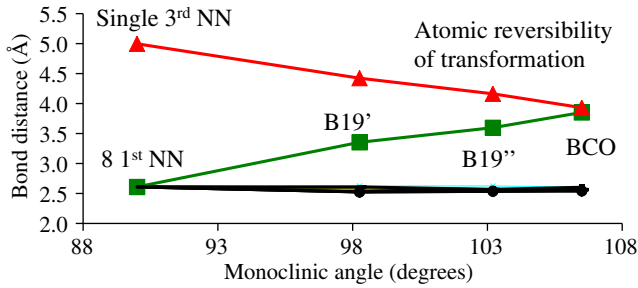


Fig. 4. Bond distance (Å) corresponding to the eight first nearest neighbors and the third nearest neighbor Ni/Ti atoms in B2, B19', B19'' and BCO plotted as a function of monoclinic angle (γ). In the case of BCO, one of the third nearest neighbors becomes identical to a first nearest neighbor. This causes the B2 \rightarrow BCO \rightarrow B2 transformation to become atomistically irreversible as the BCO variant cannot return to a unique austenite (B2) variant.

and belongs to the space group 11 or $P2_1/m$. This is a very interesting example of a phase transition between two structures belonging to the same space group; other examples of such isomorphic transformation can be found in metals (cerium, the bismuth–titanate family [29,30]) as well as molecular materials [octafluoronaphthalene [31]].

To investigate the possibility of shape memory in these phases, we next characterized whether the transformation from B2 to the various low-energy phases is atomistically reversible. Fig. 4 shows the distance between the eight first nearest neighbors (1st NN) for B2, B19', B19'' and BCO and one of the 3rd NN (Ni–Ti) whose separation decreased during the transformation. We can see how one of the eight B2 1st NN pairs increased their separation as the monoclinic angle increases while one of the 3rd NN decreased their separation. When the structure becomes BCO the distance between these two families of neighbors is identical at which point the transformation back to B2 ceases to be atomistically reversible. This is because either one of the two pairs can become 1st NN in the new austenite domain. Thus while the B2 \rightarrow BCO \rightarrow B2 phase transition is not reversible, both the B2 \rightarrow B19' \rightarrow B2 and B2 \rightarrow B19'' \rightarrow B2 transformations are reversible, and consequently both B19' and B19'' can store shape memory atomistically.

5.2. Electronic structure of the low-energy phases

As we discussed earlier, the metastable phases B19' and B19'' share the same space group and consequently one would expect the difference between them to be electronic. Fig. 5 shows the bandstructure (more accurately: the Kohn–Sham eigenenergies) for the three different phases. These three bandstructures correspond to the B19', B19'' and BCO structures in Fig. 3c, but performed with a denser k -grid of $18 \times 18 \times 18$. As described by Huang et al. [8], the transformation between B19' and BCO is associated with two high symmetry points in reciprocal space $A = [-0.5, 0.5, 0]$ and $B = [0.5, 0, 0]$. Interestingly, we find that the transition from B19' to B19'' is associated with the electron pockets at A moving above the Fermi level, whereas B states

remain below the Fermi level. Consequently, differences in electronic structure distinguish phases B19' and B19'', which are structurally equivalent.

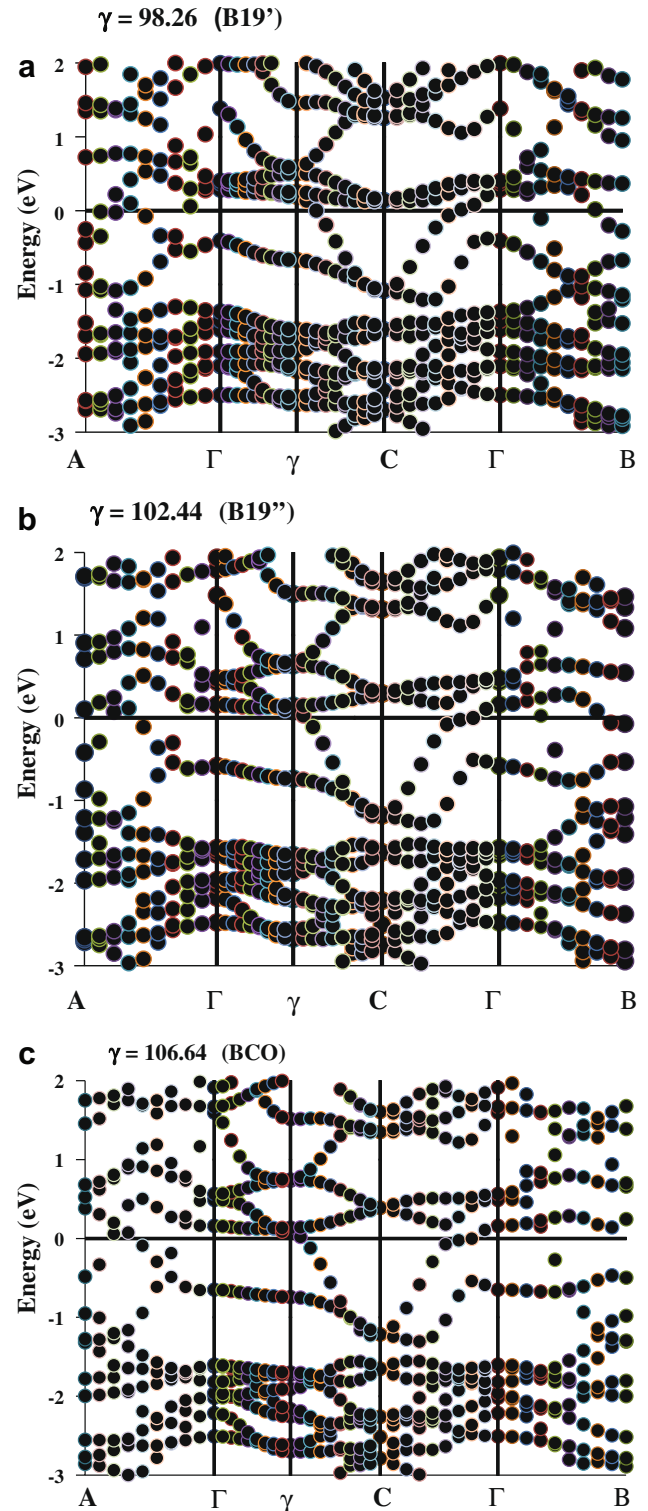


Fig. 5. Eigenenergies along different paths in reciprocal space for low-energy phases. (a) $\gamma = 98.26^\circ$ (B19'); (b) $\gamma = 102.44^\circ$ (B19''); (c) $\gamma = 106.64^\circ$ (BCO). B19'' is associated with the movement of an electron pocket at A above the Fermi level; as in BCO, electron pockets move above the Fermi level at both A and B .

6. Summary and conclusions

We used DFT within the GGA approximation to characterize key phase transformations in NiTi. Our key findings are:

- (i) We find that the B2 \rightarrow B19 transition does not involve an energy barrier. This result is in disagreement with Ref. [10], where a barrier of 13 meV/NiTi was found.
- (ii) We predict the B19 \rightarrow B19' transition to involve a small energy barrier of 1 meV/NiTi; this transition has not been studied in detail in the past.
- (iii) We predict that an intermediate phase, B19'', is involved in the homogeneous phase transformation from B19' to BCO. Huang et al. [8] predict a barrierless transition, while Wang [9] predicts a barrier significantly larger; the presence of an intermediate structure is likely to be the reason for the disagreement between the various DFT predictions regarding the B19'-BCO transition.

The presence of the B19'' phase at a monoclinic angle between those of B19' and BCO also explains the relatively low stresses necessary to stabilize B19' over BCO that leads to shape memory. This has been a significant puzzle since BCO was predicted to be the zero temperature ground state of NiTi with a relatively flat energy landscape. The presence of B19'' decreases the stress required to stabilize B19' by almost a factor of two (see Fig. 3c). It is important to mention that the relative energies between the monoclinic phases and BCO are very small, and our plane wave calculation did not predict two different monoclinic structures. However, all our calculations led to a monoclinic phase with an angle significantly larger than the one associated with the B19' martensite; this phase is likely to play a role in the stabilization of the observed structure.

The DFT calculations presented in this paper could be very useful in the development of accurate interatomic potentials for large-scale MD simulations of NiTi, which, in turn, could be useful in characterizing the role of the micro- or nanostructure on the thermo-mechanical response of NiTi. These results could also inform meso-scale phase field approaches where individual domains and their evolution are resolved [32].

Acknowledgements

This work was supported by the US Department of Energy Basic Energy Sciences (DoE-BES) program under

program number DE-FG02-07ER46399 (Program Manager: John Vetrano).

Appendix A. Supplementary material

Supplementary data associated with this article can be found, in the online version, at [doi:10.1016/j.actamat.2009.09.019](https://doi.org/10.1016/j.actamat.2009.09.019).

References

- [1] Otsuka K, Kakeshita T. *MRS Bull* 2002;91–100.
- [2] Cai W, Meng XL, Zhao LC. *Curr Opin Solid State Mater Sci* 2005;9(6):296–302.
- [3] Yuan B, Chung CY, Zhu M. *Mater Sci Eng A* 2004;382(1–2):181–7.
- [4] Humbeeck JV. *Mater Sci Eng A* 1999;273–275:134–48.
- [5] Otsuka K, Ren X. *Prog Mater Sci* 2005;50:511–678.
- [6] Bhattacharya K, Conti S, Zanzotto G, Zimmer J. *Nature* 2004;428(6978):55–9.
- [7] Huang X, Bungaro B, Godlevsky V, Rabe KM. *Phys Rev B* 2001;65:014108.
- [8] Huang X, Ackland GJ, Rabe KM. *Nat Mater* 2003;2(5):307–11.
- [9] Wang X-Q. *Phys Rev B* 2008;78:092103.
- [10] Kibey S, Sehitoglu H, Johnson DD. *Acta Mater* 2009;57(5):1624–9.
- [11] Parlinski K, Parlinska-Wojtan M. *Phys Rev B* 2002;66:064307.
- [12] Henkelman G, Uberuaga BP, Jonsson HJ. *Chem Phys* 2000;113:9901–4.
- [13] Henkelman G, Jonsson H. *J Chem Phys* 2000;113:9978–85.
- [14] Lai WS, Liu BX. *J Phys : Condens Mat* 2000;12:L53–60.
- [15] Ishida H, Hiwataru YMD. *Mol Simulat* 2007;33:459–61.
- [16] Ackland GJ, Jones AP, Noble-Eddy R. *Mater Sci Eng A* 2008;481–482:11–7.
- [17] Sato T, Saitoh K, Shinke N. *Model Simulat Mater Sci Eng* 2006;14:S39–46.
- [18] Schultz PA. *SEQQUEST code*. <http://www.dft.sandia.gov/Quest>.
- [19] Feibelman P. *J Phys Rev B* 1987;35:2626.
- [20] Feibelman P. *J Phys Rev B* 1991;44:3916.
- [21] Hohenberg P, Kohn W. *Phys Rev* 1964;136:B864.
- [22] Perdew JP, Burke K, Ernzerhof M. *Phys Rev Lett* 1996;77:3865.
- [23] Hamann DR. *Phys Rev B* 1989;40:2980.
- [24] Johnson DD. *Phys Rev B* 1988;38:12807.
- [25] Wang FE, Buehler WJ, Pickart SJ. *J Appl Phys* 1965;36(10):3232–9.
- [26] Kudoh Y, Tokonami M, Miyazaki S, Otsuka K. *Acta Metall* 1985;33(11):2049–56.
- [27] Gonze X, Beuken J-M, Caracas R, Detraux F, Fuchs M, Rignanese G-M, et al. *Comput Mater Sci* 2002;25:478–92.
- [28] Torrent M, Jollet F, Bottin F, Zerah G, Gonze X. *Comput Mater Sci* 2008;42:337.
- [29] Wilkinson MK, Child HR, McHargue CJ, Koehler WC, Wollan EO. *Phys Rev* 1961;122:1409–13.
- [30] Newnham RE, Wolfe RW, Kay MI. *Am Crystallogr Assoc* 1973 (abstract J9).
- [31] Pawley GS, Dietrich OW. *J Phys C: Solid State Phys* 1975;8:2549–58.
- [32] Bouville M, Ahluwalia R. *Phys Rev Lett* 2006;97(5):055701.